Atmos. Chem. Phys., 24, 13849–13864, 2024
https://doi.org/10.5194/acp-24-13849-2024

Atmospheric Chemistry and Physics
Open Access
EGU

Aerosol hygroscopicity over the southeast Atlantic Ocean during the biomass burning season – Part 1: From the perspective of scattering enhancement

Lu Zhang[1,2], Michal Segal-Rozenhaimer[1,3,4], Haochi Che[2,5], Caroline Dang[3,4], Junying Sun[6], Ye Kuang[7,8], Paola Formenti[9], and Steven G. Howell[10]

[1]Department of Geophysics, Porter School of the Environment and Earth Sciences, Tel Aviv University, Tel Aviv, Israel
[2]Department of Environmental Science, Aarhus University, Roskilde, Denmark
[3]Bay Area Environmental Research Institute, Moffett Field, California, USA
[4]NASA Ames Research Center, Moffett Field, California, USA
[5]Department of Geosciences, University of Oslo, Oslo, Norway
[6]State Key Laboratory of Severe Weather and Key Laboratory of Atmospheric Chemistry, Chinese Academy of Meteorological Sciences, Beijing, China
[7]Institute for Environmental and Climate Research, Jinan University, Guangzhou, China
[8]Guangdong–Hong Kong–Macau Joint Laboratory of Collaborative Innovation for Environmental Quality, Guangzhou, China
[9]Université Paris Cité and Univ Paris Est Creteil, CNRS, LISA, Paris, France
[10]Department of Oceanography, University of Hawai'i at Mānoa, Honolulu, HI, USA

Correspondence: Michal Segal-Rozenhaimer (segalrozenhaimer@baeri.org) and Haochi Che (haochi.che@geo.uio.no)

Received: 27 September 2023 – Discussion started: 12 October 2023
Revised: 16 August 2024 – Accepted: 25 October 2024 – Published: 13 December 2024

Abstract. Aerosol hygroscopicity plays a vital role in aerosol radiative forcing. One key parameter describing hygroscopicity is the scattering enhancement factor, $f(\mathrm{RH})$, defined as the ratio of the scattering coefficient at humidified relative humidity (RH) to its dry value. Here, we utilize the $f(80\,\%)$ from ORACLES (ObseRvations of Aerosols above CLouds and their intEractionS) 2016 and 2018 airborne measurements to investigate the hygroscopicity of aerosols, its vertical distribution, its relationship with chemical composition, and its sensitivity to organic aerosol (OA) hygroscopicity over the southeast Atlantic (SEA) Ocean during the biomass burning (BB) season.

We found that aerosol hygroscopicity remains steady above 2 km, with a mean $f(80\,\%)$ of 1.40 ± 0.17. Below 2 km, aerosol hygroscopicity increases with decreasing altitude, with a mean $f(80\,\%)$ of 1.51 ± 0.22, consistent with higher values of BB aerosol hygroscopicity found in the literature. The hygroscopicity parameter of OA (κ_{OA}) is retrieved from the Mie model with a mean value of 0.11 ± 0.08, which is in the middle to upper range compared to the literature. Higher OA hygroscopicity is related to aerosols that are more aged, oxidized, and present at lower altitudes. The enhanced biomass burning aerosol (BBA) hygroscopicity at lower altitudes is mainly due to a lower OA fraction, increased sulfate fraction, and greater κ_{OA} at lower altitudes.

We propose a parameterization that quantifies $f(\mathrm{RH})$ with chemical composition and κ_{OA} based on Mie simulation of internally mixed OA–$(NH_4)_2SO_4$–BC mixtures. The good agreement between the predictions and the ORACLES measurements implies that the aerosols in the SEA during the BB season can be largely represented by the OA–$(NH_4)_2SO_4$–BC internal mixture with respect to the $f(\mathrm{RH})$ prediction. The sensitivity of $f(\mathrm{RH})$ to κ_{OA} indicates that applying a constant κ_{OA} is only suitable when the OA fraction is low and κ_{OA} shows limited

variation. However, in situations deviating these two criteria, κ_{OA} can notably impact scattering coefficients and aerosol radiative effect; therefore, accounting for κ_{OA} variability is recommended.

1 Introduction

Aerosol hygroscopicity is an important physicochemical property of atmospheric aerosols, representing the extent to which particles take up water when exposed to a certain relative humidity (RH) (Covert et al., 1972). Key parameters describing aerosol hygroscopicity include the scattering enhancement factor, f(RH), which represents the enhancement of the aerosol light-scattering coefficient as a function of RH (Carrico et al., 2003), and κ, the hygroscopicity parameter, whose value is defined by its effect on the water activity of the solution (Petters and Kreidenweis, 2007). Water uptake will increase the size and the mass of hygroscopic aerosols, alter their refractive index, enhance the scattering ability, and ultimately influence the single-scattering albedo and aerosol radiative forcing (Cotterell et al., 2017; Titos et al., 2021; Zieger et al., 2013). Furthermore, hygroscopicity affects aerosols' ability to act as CCN (cloud condensation nuclei) and ice nuclei and further influences cloud properties and precipitation (Cai et al., 2021; Che et al., 2017; Ervens et al., 2007). Climate model results show that even a modest change in κ_{OA} (κ of organic aerosols) can lead to significant changes in CCN, droplet number concentration, and aerosol radiative effects (Liu and Wang, 2010; Rastak et al., 2017). The treatment of aerosol hygroscopicity is one of the key factors contributing to discrepancies between model simulations and observations and among model estimates (Burgos et al., 2020; Haywood et al., 2008; Reddington et al., 2019).

Africa emits $\sim 1/3$ of the Earth's annual biomass burning (BB) emissions (van der Werf et al., 2010), and its burned areas are increasing every year (Ramo et al., 2021). Each austral spring (July to October), BB aerosols (BBAs) from African fires are transported westward through the free troposphere (FT) over the persistent stratocumulus cloud deck in the southeast Atlantic (SEA) and eventually subside into the marine boundary layer (MBL) (Redemann et al., 2021). BBAs undergo atmospheric processing during transport, altering their chemical composition, oxidation extent, particle polarity, molecular weight, volatility, and solubility (Rastak et al., 2017), making the hygroscopicity highly variable. Laboratory studies show that minutes-old BBA are more hygroscopic than hour-old BBA (Day et al., 2006), while the hygroscopicity of BBA transported for more than several days in the SEA region remains an area of investigation. Furthermore, these BBAs mix with pristine aerosols and are subject to marine influences from the SEA, resulting in a distinct vertical variation of aerosol hygroscopicity.

The hygroscopicity of organic aerosol (OA), the dominant component of aerosols in most cases, is poorly characterized due to its chemical complexity (Kuang et al., 2020a; Mei et al., 2013). Values of κ_{OA} can range from 0 for hydrophobic freshly emitted organics to approaching 1.0 for very hygroscopic amino acids (Kuang et al., 2020a; Petters et al., 2009; Zhang et al., 2007). Biomass burning organic aerosols (BBOAs) are usually regarded as hydrophobic, while the mass fraction of aged BBOA shows a positive correlation with κ_{OA} (Cerully et al., 2015; Kuang et al., 2021). Several studies have found a linear correlation between OA hygroscopicity and its oxidation level, commonly characterized by the oxygen-to-carbon (O / C) ratio or the fraction of total organic mass spectral signal at m/z 44 (f_{44}) (Lambe et al., 2011; Mei et al., 2013). However, this linear relationship is not always established, especially for secondary OA with a lower O / C ratio under subsaturated conditions, for which solubility may play a more important role. In addition, studies show that molecular weight, surface tension, and liquid–liquid phase separation are also related to the water affinity of OA (Liu et al., 2018; Rastak et al., 2017; Wang et al., 2019), all contributing to the complexity of OA hygroscopicity.

The ORACLES (ObseRvations of Aerosols above CLouds and their intEractionS) campaign (Redemann et al., 2021) provides a comprehensive observation of aerosols above the SEA Ocean with 4–12 d of transport from Africa fires, making it a valuable opportunity to investigate the hygroscopicity of aged BBAs and their OA. In this paper, we first characterize the aerosol hygroscopicity and its vertical distribution over the SEA during the BB season, then propose a parameterization relating aerosol hygroscopicity to chemical composition and k_{OA}, and finally evaluate the sensitivity of aerosol hygroscopicity to k_{OA}. Results are expected to provide a reference to the treatment of aerosol hygroscopicity in climate models and satellite retrievals and to contribute to aerosol–cloud interactions and radiative assessments in this climatically important SEA region.

2 Methods

2.1 Aircraft instrumentation and data analysis

We analyzed airborne, in situ data measured over the SEA region from the ORACLES campaign performed in September 2016 and October 2018 (Redemann et al., 2021). The flight tracks are shown in Fig. 1. All instruments were deployed on the NASA P-3 aircraft. Aerosol particles were introduced into the P-3 via the solid diffuser inlet. The inlet was operated isokinetically by matching the flow rate to the external airflow velocity to within 5 % (Dobracki et al., 2023). This inlet was designed to effectively transfer parti-

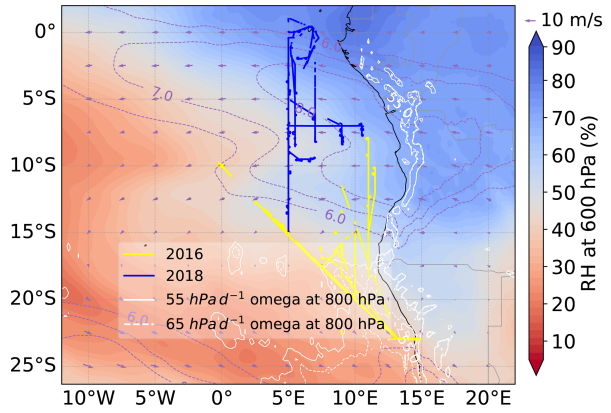

Figure 1. Flight tracks for the 2016 and 2018 ORACLES campaigns. Map of October mean ERA5 600 hPa RH overlaid by the 600 hPa zonal wind (purple contours; 6, 7, and 8 m s^{-1}), 600 hPa horizontal wind vector (purple arrows; m s^{-1}), and ORACLES flight tracks in 2016 (yellow) and 2018 (blue). White contours are the 2016 September mean vertical velocity, omega, at 800 hPa. Solid and dashed lines represent the subsidence of 55 and 65 hectopascals per day (hPa d^{-1}).

cles up to 4.0 µm in dry diameter (McNaughton et al., 2007). The inner pipework was designed for minimal transport losses for particles up to 4.0 µm using an online particle loss calculator (Aerosol Calculator, https://tsi.com/getmedia/540a30fa-8444-49f6-814f-891495c70aa1/Aerocalc2001_1, last access: 12 December 2024). Two Radiance Research M903 integrating nephelometers (Nephs) were operating in parallel, one (referred to as the "reference Neph") under relatively dry conditions and the other (known as the "humidified Neph") maintained at ∼80 % RH. Particles entering the reference Neph were heated to the aircraft cabin temperature, significantly reducing their RHs in the Neph and resulting in most particles having an RH below 35 %. The humidified Neph was situated downstream of a humidifier, which maintained the RH at the inlet of the Neph at ∼80 % within a few percent, as detailed in Howell et al. (2006). The RH probes in M903 were corrected based on lab calibrations and the RH errors are roughly 3 %. The temperature errors are about 0.5 °C. Measurements were reported at 1 Hz. For the calculation of f(RH), data with a reference Neph RH greater than 35 % or a humidified Neph RH smaller than 76 % were excluded. The distributions of the RHs of both the reference and humidified Nephs used in this study are shown in Fig. S3 in the Supplement. Calibrations were performed in the field with refrigerant R-134A (1,1,1,2-tetrafluoroethane). Truncation correction was performed for both Nephs according to Anderson and Ogren (1998). All scattering coefficients and scattering enhancement factors are reported at 540 nm wavelength.

The non-refractory submicron aerosol composition was provided by a high-resolution time-of-flight aerosol mass spectrometer (HR-ToF-AMS, Aerodyne Research Inc.) (Dobracki et al., 2023). The fragment analysis provided f_{44} and f_{60}, representing the fractions of the OA mass spectrum signals at $m/z = 44$ (mainly CO_2^+) and $m/z = 60$ (mainly $C_2H_4O_2^+$), respectively, in the total OA mass. The mass concentration of refractory BC was provided by a single-particle soot photometer (SP2, Droplet Measurement Technology; Sedlacek et al., 2022).

The dry particle number size distribution (PNSD) of PM_1 was provided by an ultrahigh-sensitivity aerosol spectrometer (UHSAS, Droplet Measurement Technology). The UHSAS measures particles between 60 and 1000 nm in optical diameter. It was calibrated with polystyrene latex (PSL) spheres, whose real refractive index n is 1.572 at the UHSAS laser wavelength (Howell et al., 2021). The UHSAS undersized particles in BB plumes; the undersized data were corrected to mobility diameter according to Howell et al. (2021). The PNSD of supermicron particles was measured by an aerodynamic particle sizer (APS). The aerodynamic diameter of the APS was converted to the volume equivalent diameter according to DeCarlo et al. (2004). Particles were assumed to be spherical (shape factor = 1) with a density of 1.5 g cm^{-3}. However, since the supermicron particles made a minimal contribution to the total scattering coefficient, we have neglected the supermicron particles, and only UHSAS measurements are used in this study. The minor contribution of supermicron particles to the total scattering coefficients is described and illustrated in Sect. S1 and Fig. S1 in the Supplement. The plume age was modeled with a 2-week forecast using the Weather Research and Aerosol Aware Microphysics (WRF-AAM) model (Thompson and Eidhammer, 2014). Carbon monoxide was tagged as a tracer at the fire source, identified by a burned area product from the moderate resolution imaging spectrometer with a 500 m spatial resolution.

All measurements were averaged to 15 s and adjusted to standard temperature and pressure at 273.15 K and 1013 hPa. Data with scattering coefficient < 10 Mm^{-1} are not included. The final measurements used in this study have an average RH of 79 ± 0.5 % for the humidified Neph and RH < 30 % for the reference Neph. To ensure the influence of BB emissions, only data with $f_{60} > 0.003$ are considered (Cubison et al., 2011). This study analyzes measurements from 21 flights, totaling approximately 134 flight hours after applying the abovementioned constraints.

2.2 Calculation of f(RH) and γ parameterization

The aerosol scattering enhancement factor, f(RH), is calculated as

$$f(\mathrm{RH}) = \frac{\sigma_{\mathrm{sp}}(\mathrm{RH})}{\sigma_{\mathrm{sp}}(\mathrm{RH_{ref}})}, \quad (1)$$

where σ_{sp}(RH) and $\sigma_{\mathrm{sp}}(\mathrm{RH_{ref}})$ represent the scattering coefficients at humidified and reference Neph RHs, respectively. Note that the f(RH) only includes those with reference Neph

RHs equal to or smaller than 35 % to facilitate comparison with previous studies. For simplicity, we denote the $f(\mathrm{RH})$ at the RH of humidified Neph as $f(80\,\%)$, despite the small variation of the RH in humidified Neph. The $f(\mathrm{RH})$ is usually fitted to a γ parameterization to apply to a more extensive RH range (Sheridan et al., 2002; Titos et al., 2016).

$$f(\mathrm{RH}) = \left(\frac{1-\mathrm{RH}/100}{1-\mathrm{RH}_{\mathrm{ref}}/100}\right)^{-\gamma} \quad (2)$$

In our case, the γ was calculated with the RH and $\mathrm{RH}_{\mathrm{ref}}$ using Eq. (2) since the $f(\mathrm{RH})$ was only measured at a fixed RH.

2.3 Modeling of $f(\mathrm{RH})$

The $f(\mathrm{RH})$ can be modeled with Mie theory (Mie, 1908). The Python package PyMieScatt (Sumlin et al., 2018), an implementation of Mie theory, was applied in this study. Inputs of PyMieScatt include PNSD and complex refractive index. Dry particles beyond PM_1 (particulate matter with an aerodynamic diameter less than 1 µm) are not included in this calculation, supported by their minor contribution to the total scattering, as discussed in Sect. S1 of the Supplement. A volume mixing rule was used to calculate the refractive index. The volume of inorganic salts was converted from those of $\mathrm{SO_4^{2-}}$, $\mathrm{NO_3^-}$, and $\mathrm{NH_4^+}$ from AMS following a modified ion-pairing scheme (Gysel et al., 2007; Zhang et al., 2022). Good agreement has been achieved for calculated and measured scattering coefficients under dry conditions, which indicates good data quality and provides the basis for calculating $f(\mathrm{RH})$ and retrieving $\kappa_{f(\mathrm{RH})}$. The comparison between calculated and measured scattering coefficients is shown in Fig. S4 in the Supplement. By combining the Mie model with κ-Köhler theory, we can then calculate the scattering coefficients under humidified RH conditions. For more details of the calculation, refer to Zieger et al. (2013). Subsequently, $f(\mathrm{RH})$ and γ can be obtained using Eqs. (1) and (2). The theoretically calculated $f(\mathrm{RH})$ in Sect. 3.3.1 and 3.3.2 used an assumed PNSD and different chemical composition combinations. One assumed PNSD was used in these calculations due to its minor impact on $f(\mathrm{RH})$, which is discussed in detail in Sect. S2 in the Supplement.

2.4 $\kappa_{f(\mathrm{RH})}$ retrieval and κ_{OA} calculation

The aerosol hygroscopicity parameter κ can be retrieved from $f(\mathrm{RH})$, usually denoted as $\kappa_{f(\mathrm{RH})}$ (Chen et al., 2014). It can be regarded as the scattering-coefficient-weighted average κ (Kuang et al., 2021). Specifically, we iteratively adjust $\kappa_{f(\mathrm{RH})}$ to minimize the difference between the calculated and measured $f(\mathrm{RH})$. Detailed descriptions of the retrieval procedure of $\kappa_{f(\mathrm{RH})}$ can be found in Chen et al. (2014).

According to Petters and Kreidenweis (Petters and Kreidenweis, 2007), the overall κ_{chem}, which is defined as the κ for the whole aerosol population, can also be calculated from various chemical compositions following the ZSR (Zdanovskii–Stokes–Robinson) mixing rule. Kuang et al. (2020b) thoroughly outline in their Sect. 3.3 that the $\kappa_{f(\mathrm{RH})}$ can accurately represent the κ_{chem} of PM_1. Therefore, the hygroscopicity parameter of OA, κ_{OA}, can be calculated as

$$\kappa_{\mathrm{OA}} = \frac{\kappa_{f(\mathrm{RH})} - \left(\sum_{i=\mathrm{inorg}} \kappa_i \varepsilon_i + \kappa_{\mathrm{BC}} \varepsilon_{\mathrm{BC}}\right)}{\varepsilon_{\mathrm{OA}}}, \quad (3)$$

where inorg represents inorganic salts, which were derived from the $\mathrm{SO_4^{2-}}$, $\mathrm{NO_3^-}$, and $\mathrm{NH_4^+}$ ions measured from AMS following a modified ion-pairing scheme (Gysel et al., 2007; Zhang et al., 2022). The subscript i denotes each individual inorganic salt. ε represents the volume fraction of each component, calculated as the ratio of the volume of each component to the volume of PM_1. The PM_1 volume is computed as the sum of the volumes of inorganic salts, OA, and BC. The hygroscopic parameter κ and density used in this study can be found in Table S1.

3 Results and discussion

3.1 Overview of chemical compositions in 2016 and 2018 during ORACLES

Flights during ORACLES in 2016 (Fig. 1, yellow lines) are in the region of 8–24° S and 0–15° E, traversing both the southern African Easterly Jet (AEJ-S) region and the continent anticyclone (Ryoo et al., 2021). As a result, aerosols around 3–4 km in 2016 during ORACLES include both less aged (< 4 d) particles coming directly from the continent and highly aged (> 10 d) particles transported from the west and north, resulting in a larger variation of plume age in each level as shown in Fig. 2a. At lower altitudes, aerosols are less aged than those in the 2018 campaign due to the subsidence (positive values of omega) near the Namibian coast (Fig. 1). During the 2016 campaign, the cloud top is generally below 1.5 km. The 2018 ORACLES flights, represented by blue lines in Fig. 1, are primarily situated within the 0–15° S and 5–10° E coordinates. The cloud top in this region is a bit lower than in the 2016 campaign, centering around 1 km. This area generally coincides with the region influenced by the southern African Easterly Jet (AEJ-S). BBAs are lifted up to the free troposphere, are transported westward by the AEJ-S, and then subside into the marine boundary layer, rendering the distinct vertical age pattern that increases with decreasing altitude (Fig. 2c). Correspondingly, aerosols in the SEA region during the BB season exhibit a distinct vertical distribution of chemical composition. From Fig. 2b and d, the vertical profiles of chemical composition fractions are generally consistent during the 2016 and 2018 ORACLES campaigns. In this section, we focus on the variation of OA and sulfate, two components that dominate aerosol hygroscopicity in the SEA.

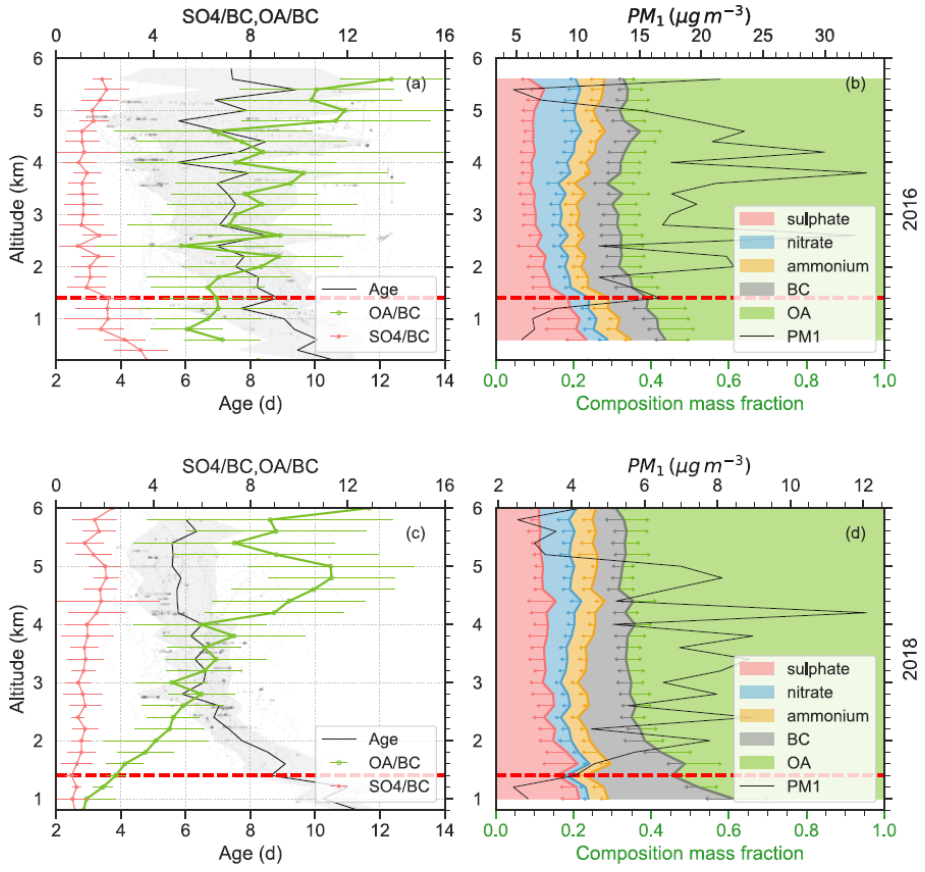

Figure 2. The vertical distribution of plume age and chemical composition. **(a, c)** Variation of plume age (black), OA / BC, and SO_4 / BC with altitude in the 2016 **(a)** and 2018 **(c)** ORACLES campaigns. Gray dots show the distribution of the plume age with altitude. **(b, d)** The average vertical distribution of the mass ratio of chemical compositions and the average mass concentration of PM_1 from AMS and SP2 in every 200 m in the 2016 and 2018 ORACLES campaigns, respectively. The lines are the mean value in every 200 m bin. Error bars and gray shading represent the standard deviation in every 200 m bin. The dashed red lines at 1400 m show the maximum height of the MBL during the study period.

OA constitutes the largest fraction of aerosol mass in ORACLES, approximately 60 %. The OA mass fraction in both years shows little variation above 2 km; below this altitude, OA mass fraction decreases with decreasing altitude, in contrast to the trend of the sulfate mass fraction. The OA / BC ratio, representing the OA mass concentration normalized by that of BC to remove the dilution effect during transport and an indication of OA processing, differs in 2016 and 2018. While 2018 data show a clear decrease in OA / BC with decreasing altitude, the decrease was less pronounced in 2016, showing considerable variation at identical altitudes. Meanwhile, OA / BC shows a clear reverse trend with the plume age in 2018; this inverse relationship is less obvious in 2016. Dobracki et al. (2023) used RH as an indicator to investigate the importance of thermodynamic partitioning in OA / BC changes during the 2016 ORACLES campaign, concluding that it accounts for no more than 10 % of the changes. The dominant factor is believed to be the oxidation of OA through fragmentation. A similar result is found in this study using temperature as an indicator, as shown in Fig. 3a. Please note that Fig. 3 only considers OA above 1.4 km and temperature $> 0\,^{\circ}C$ to minimize the marine influence and to exclude possible ice nucleation. The OA / BC ratio in the 2016 ORACLES campaign did not show a clear decrease with increasing temperature, as NO_3 / BC did, which is a result of thermodynamic repartition to the gas phase. However, in the 2018 ORACLES campaign, we did notice a significant decrease in OA / BC with increasing temperature (Fig. 3b). The OA / BC decreased $\sim 70\,\%$ from 9.7 ± 3.1 for temperature 0–4 °C to 2.9 ± 0.9 for temperature $> 20\,^{\circ}C$, only slightly lower than the decrease in NO_3 / BC of $\sim 85\,\%$. Yet, we cannot simply attribute the OA / BC changes to thermodynamic repartition while disregarding the effect of aging or OA oxidation. In 2018, temperature and plume age are closely correlated (Pearson correlation coefficient of 0.51), and the decrease in OA / BC is accompanied by aging (Pearson correlation coefficient of 0.57), as shown in Fig. 2a and b. We utilized the oxidation

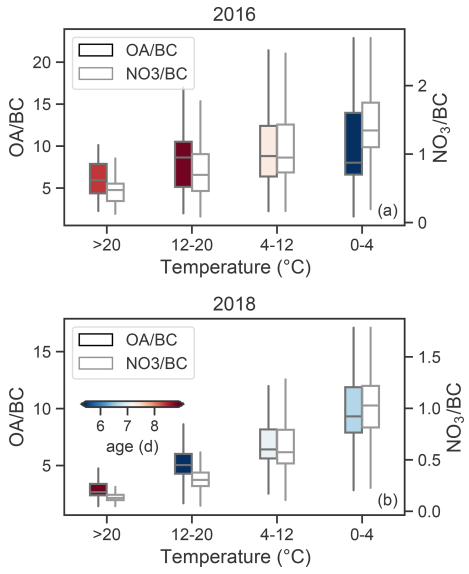

Figure 3. OA / BC (black outline) and NO_3 / BC (gray outline) mass ratios as a function of ambient temperature in the 2016 **(a)** and 2018 **(b)** ORACLES campaigns for altitude > 1.4 km and temperature > 0 °C. The boxes represent the 10th percentile, 25th percentile, median, 75th percentile, and 90th percentile.

state to differentiate between the effects of thermodynamic repartition and OA oxidation. Figure 4 shows van Krevelen diagrams (H / C vs. O / C; Ng et al., 2011) for aerosols at temperatures > 20 and 0–4 °C. The estimated carbon oxidation state (OS_C), defined as $OS_C = 2O/C - H/C$, can also indicate different OA volatility regimes, with OS_C of −2.0 to −1.5 for HOA (hydrocarbon-like OA), −1.75 to −0.75 for BBOA (biomass burning OA), −1.0 to 0.0 for SV-OOA (semi-volatile oxidized OA), and 0.0 to 1.0 for LV-OOA (low-volatility oxidized OA) (Donahue et al., 2012; Kroll et al., 2011). If thermodynamic repartition plays a more crucial role, the OA remaining under higher temperature would be less volatile due to evaporation of more volatile OA. Notably, we found the opposite. From Fig. 4, aerosols at temperatures > 20 °C (lower altitudes) are generally more volatile than those at temperatures 0–4 °C (higher altitudes). This indicates that thermodynamic repartition is not a dominant factor in OA / BC changes and that the OA oxidation through fragmentation is more important in OA / BC changes in 2018, consistent with the 2016 campaign as well as results in Dobracki et al. (2023). This is also in line with the findings of Dang et al. (2022), who found fewer organics in aerosols collected on filters associated with more aged plumes and more rounded and viscous organics on filters sampled from less-aged plumes. For OA below 1.4 km, aqueous-phase reactions and cloud scavenging might also contribute to the loss of OA during entrainment and within the MBL (Che et al., 2022a; Wu et al., 2020).

The variation of sulfate mass fraction remains largely constant above 2 km, and below 2 km, it increases with decreasing altitudes. The higher sulfate fraction at lower altitudes is consistent with the observations from the CLARIFY-2017 (CLoud–Aerosol–Radiation Interaction and Forcing for Year 2017) campaign (Wu et al., 2020), which was conducted downwind of ORACLES in the SEA ocean. This higher sulfate fraction at lower altitudes results from the increase in SO_4 / BC and decrease in OA / BC. The SO_4 / BC ratio generally remains constant above 800 m in both years' campaigns. However, for the 2016 ORACLES campaign, where there are samples below 800 m, the ratio shows an increase with decreasing altitude. This increase could indicate a sulfate contribution from the ocean, either in the form of sea-salt sulfate or through the oxidation of dimethylsulfide (DMS) emitted by marine phytoplankton. The latter can contribute to non-sea-salt sulfate by oxidizing to SO_2 and further to sulfate (Mayer et al., 2020; Alexander et al., 2005). Notably, part of the 2016 flight region, especially the SEA offshore of Namibia, is known as an upwelling region with high DMS emissions (Andreae et al., 1995). Klopper et al. (2020) have attributed 57 % of sulfate to sea salt and 43 % to non-sea-salt sulfate along the Namibian coast. These findings align with model simulations showing that DMS is the third-largest CCN source in the SEA up to 2 km (Che et al., 2022b).

Furthermore, BC mass constitutes approximately 10 % of the PM_1 mass fraction, indicating the large influence of BB in this region. The nitrate mass fraction increases with increasing altitude in all layers, which is consistent with the findings of CLARIFY and can be explained by the shift of gas–particle partitioning of the HNO_3–NH_3–NH_4NO_3 system towards the aerosol phase at the lower temperatures found at higher altitudes (Wu et al., 2020). The mass fraction of ammonium stays stable with height at approximately 5 %. We neglected chloride in this study as it accounts for less than 1 ± 1 % of the mass fraction.

3.2 Aerosol hygroscopicity in SEA in 2016 and 2018 during ORACLES

In general, the aerosol hygroscopicity stays stable above 2 km in both years' campaigns, while below 2 km, aerosols become more hygroscopic at lower altitudes (Fig. 5). The results from the Levene test for medians for $f(80\,\%)$, $\kappa_{f(\mathrm{RH})}$, and κ_{OA} indicate that $f(80\,\%)$, $\kappa_{f(\mathrm{RH})}$, and κ_{OA} are statistically different above and below 2 km, with a confidence level of 95 %. This is consistent with the vertical variation of sulfate and OA mass fraction, i.e., more sulfate and less OA at lower altitudes (Fig. S5). The probability density function (PDF) distributions of $f(80\,\%)$ and $\kappa_{f(\mathrm{RH})}$ are similar in the 2016 and 2018 campaigns, with larger variations and higher values of the aerosol hygroscopicity PDF under 2 km (Fig. 5d and e). For $f(80\,\%)$ below 2 km, a primary mode with a value of around 1.45 is evident, but there is also a second mode with a value of around 1.81 for aerosols in both

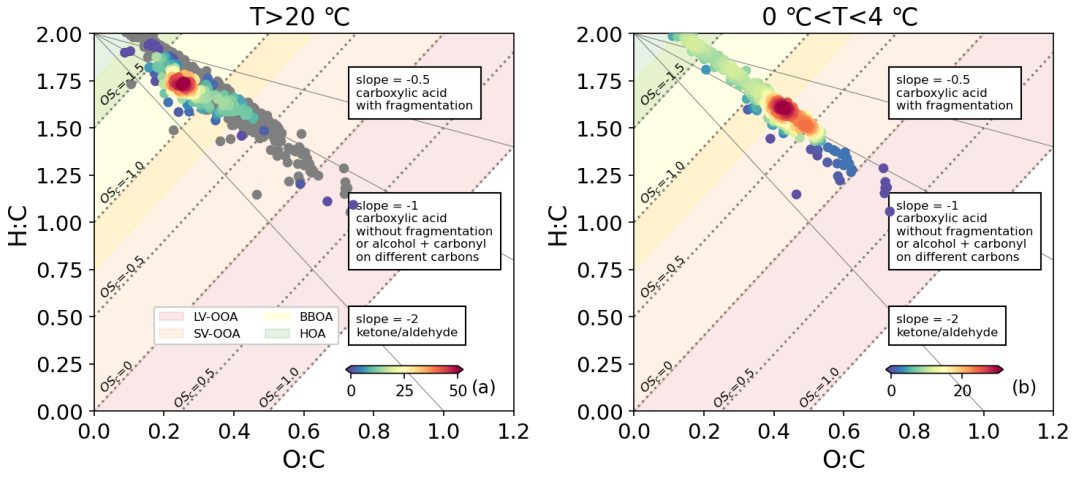

Figure 4. Van Krevelen diagram (H / C vs. O / C) for aerosols with temperatures higher than 20 °C **(a)** and with temperatures lower than 4 °C **(b)**. The color scale indicates the density of the data in each plot. The gray dots in panel **(a)** are the van Krevelen diagram of aerosols with temperatures lower than 4 °C, the same as panel **(b)**.

years. While the second mode is subtle, it can be identified in the PDF of $\kappa_{f(\mathrm{RH})}$ (Fig. 5e). This suggests the presence of highly hygroscopic substances and could indicate a marine influence, as most aerosols below 2 km are within the MBL. For aerosols above 2 km, the mean and standard deviation of $f(80\,\%)$ and $\kappa_{f(\mathrm{RH})}$ are 1.40 ± 0.17 and 0.19 ± 0.07, respectively (Fig. 5, Tables 1 and S2). These values indicate less-hygroscopic particles (Liu et al., 2011) and are lower than those for marine aerosols (Zieger et al., 2010; Carrico et al., 2003) but higher than those for dust and polluted dust particles (Bukowiecki et al., 2016; Zhang et al., 2015). They are comparable to smoke-dominated aerosols, such as the smoke from savanna fires in Australia (Gras et al., 1999) and the BBA from forest fires in the northeast US (Wang et al., 2007). These values are slightly higher than the $f(80\,\%)$ in Brazil (SCAR-B) (Kotchenruther and Hobbs, 1998). The particles below 2 km are more hygroscopic (Liu et al., 2011). The mean and standard deviation of $f(80\,\%)$ and $\kappa_{f(\mathrm{RH})}$ are 1.51 ± 0.22 and 0.23 ± 0.08, respectively, placing them in the upper ranges of BBA hygroscopicity reported in the literature. These values are comparable to those of the aged smoke in Africa (SAFARI; Magi and Hobbs, 2003) and at the Yangtze River Delta background station (Zhang et al., 2015). They match the $\kappa_{f(\mathrm{RH})}$ of 0.22 at a rural site in southern China (Kuang et al., 2021) but are lower than the values for BBA in East Asia (ACE-Asia; Kim et al., 2006) and agricultural burning in INDOEX (Indian Ocean Experiment; Sheridan et al., 2002). Comparing to the κ obtained from CCN measurements at a similar location in August 2017 ORACLES (Kacarab et al., 2020), our results are $\sim 30\,\%$ lower. This difference is expected because κ values obtained under supersaturated conditions are typically larger than those from subsaturated conditions (Petters and Kreidenweis, 2007). This highlights the significance of using the appropriate κ for subsaturated and supersaturated investigations, such as when examining aerosol liquid water content and cloud condensation nuclei activation (Rastak et al., 2017; Petters and Kreidenweis, 2007).

The mean κ_{OA} (± 1 standard deviation) is 0.11 ± 0.08, with 25th and 75th percentiles of 0.06 and 0.16. From the vertical profiles, more hygroscopic OA is generally more aged, highly oxidized, and usually located at lower altitudes (Figs. 2 and 5). In addition, we observed a slight increase in κ_{OA} with volatility in 2016, with a Pearson correlation coefficient of -0.35 between κ_{OA} and $\mathrm{OS_C}$, contrasting with the conventional understanding that the most volatile compounds have the least hygroscopicity. This trend has been observed, albeit rarely, in field and laboratory studies (e.g., Cerully et al., 2015; Asa-Awuku et al., 2008). It may be related to fragmentation during OA oxidation, where highly aged and low-volatility OA may dissociate into more volatile fragments that are still highly functionalized and hygroscopic. However, in general, no clear correlation has been found for κ_{OA} with altitude or oxidation level.

We noted a portion of highly aged aerosols (> 10 d) in 2016 having high OA / BC (> 12, corresponding OA mass fraction $> 50\,\%$), in contrast to the general trend that more aged aerosols correspond to smaller OA / BC (Fig. 2). About 95 % of these aerosols are above 3 km and have a slightly lower f_{44} than the campaign average (Fig. S6a). Approximately 60 % belong to LV-OOA with $\mathrm{OS_C} > 0$ and 40 % are SV-OOA (Fig. S6b). As shown in Fig. S6c, the κ_{OA} values are smaller for these aerosols compared to the whole 2016 campaign, which is consistent with previous studies finding that κ_{OA} is lower for less-oxidized OA (Kuang et al., 2020a; Rastak et al., 2017; Mei et al., 2013), though we do not observe such correlation for the entire campaign. We hypothesize that thermodynamic repartitioning has played a role, i.e.,

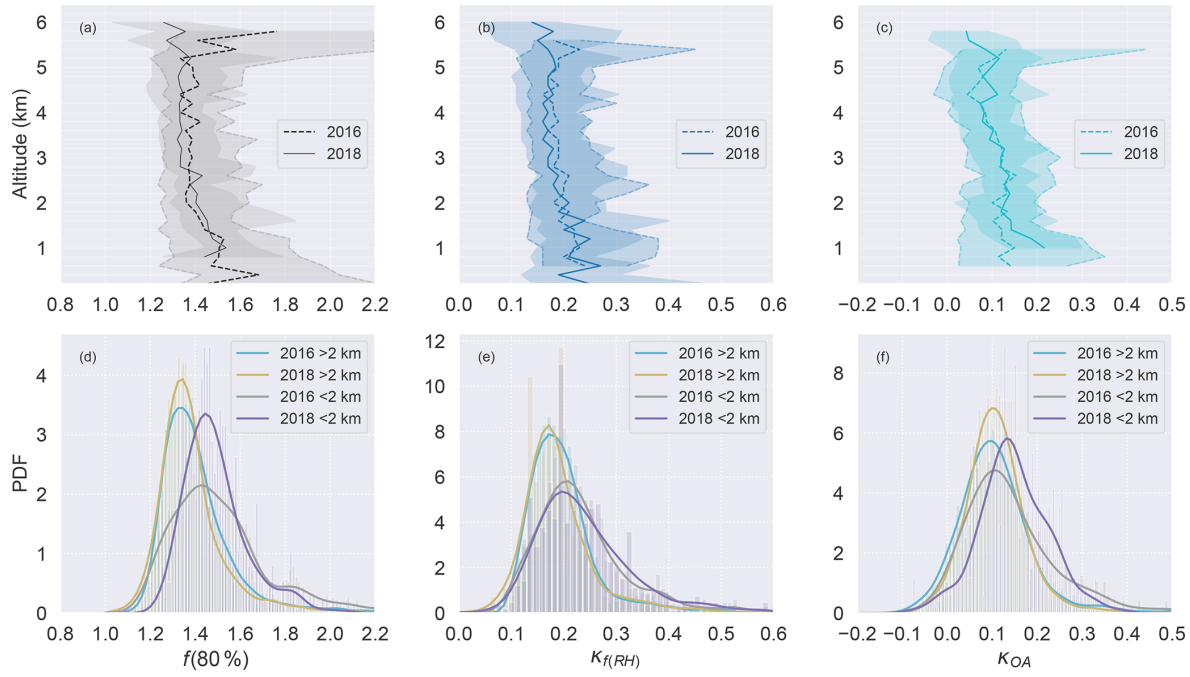

Figure 5. Vertical profiles and PDF of $f(80\,\%)$ **(a, d)**, $\kappa_{f(\mathrm{RH})}$ **(b, e)**, and κ_{OA} **(c, f)** for aerosols in the 2016 (dotted line) and 2018 (solid line) ORACLES campaign. The lines in panels **(a)–(c)** represent the medians, and the shading in panels **(a)–(c)** represents the 10th and 90th percentiles.

Table 1. The $f(\mathrm{RH})$ of biomass burning aerosol from the literature.

$f(\mathrm{RH})$	RH	Location	Fuel type and notes	Reference
1.37	80 %	Australia	light-wooded savanna fires	Gras et al. (1999)
1.40	82 %	northeast US	forest fires	Wang et al. (2007)
1.16	80 %	Brazil (SCAR-B[a])	grass, shrub, and trees	Kotchenruther and Hobbs (1998)
1.44 ± 0.02	80 %	southern Africa (SAFARI 2000[b])	aged heavy smoke	Magi and Hobbs (2003)
1.60 ± 0.20	85 %	Korea (ACE-Asia[c])	BBA	Kim et al. (2006)
1.58 ± 0.21	85 %	Indian Ocean (INDOEX[d])	agricultural burning	Sheridan et al. (2002)
1.51 ± 0.22	80 %	southeast Atlantic Ocean (below 2 km, ORACLES)	savanna[e]	This study
1.40 ± 0.17	80 %	southeast Atlantic Ocean (above 2 km, ORACLES)	savanna[e]	This study

[a] Smoke, Clouds, and Radiation-Brazil. [b] Southern African Regional Science Initiative 2000. [c] Aerosol Characterization Experiment. [d] Indian Ocean Experiment. [e] Fuel type discussed in Che et al. (2022c).

less-oxidized materials condensed onto pre-existing OA under low temperature at high altitudes, resulting in smaller f_{44} values and contributing to SV-OOA. These less-oxidized materials are generally less functionalized and less hygroscopic, which would lead to a lower κ_{OA}.

3.3 Relationship with chemical composition and κ_{OA}

3.3.1 Comparison with various campaigns

Quinn et al. (2005) proposed a parameterization quantifying the relationship between γ and F_{O}, the ratio of mass concentrations of OA to OA and $\mathrm{SO_4^{2-}}$, based on measure-

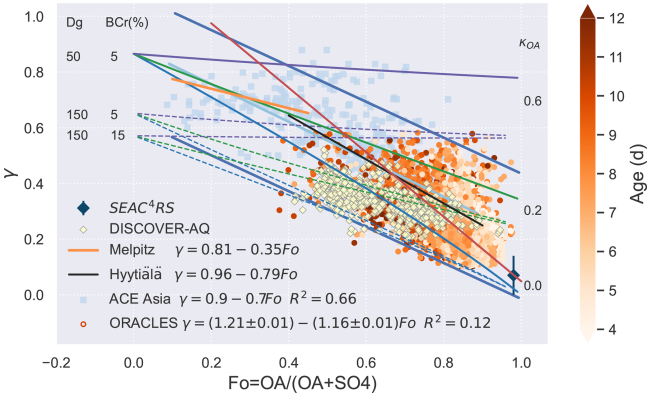

Figure 6. γ versus F_O in various campaigns and for internally mixed OA–$(NH_4)_2SO_4$–BC mixtures. F_O represents the ratio of mass concentrations of OA to OA and SO_4^{2-}. Solid lines in light blue and red represent the linear fits for ACE-Asia and ORACLES, respectively. Solid blue lines show the 95 % prediction bands for the ACE-Asia data, in light blue rectangles, taken from Quinn et al. (2005). The color bar represents the plume age (days) in ORACLES. Data for SEAC^{4}RS are shown by a dark blue diamond, taken from Shingler et al. (2016). DISCOVER-AQ data are shown by yellow diamonds, taken from the NASA Langley Research Center Atmospheric Science Data Center (NASA/LARC/SD/ASDC, 2022). Fitting lines for two European sites in Melpitz (solid orange line) and Hyytiälä (solid black line) are from Zieger et al. (2015). Blue, green, and purple lines represent results for internally mixed OA–$(NH_4)_2SO_4$–BC mixtures with (1) a range of BC mass fraction (BCr, solid for 5 % and dashed for 25 %) and (2) OA with κ_{OA} of 0 (blue), 0.2 (green), and 0.6 (purple) from Mie calculations assuming a lognormal size distribution with a geometric mean diameter D_{gn} of 150 nm and a standard deviation σ_{sg} of 1.6.

ments in ACE-Asia. We applied the parameterization to ORACLES measurements, and as shown in Fig. 6, our data are well within the 95 % prediction confidence intervals. We further investigated the γ–F_O dependence of BBA from DISCOVER-AQ and SEAC^{4}RS (Shingler et al., 2016) as well as continental aerosols from the central European station in Melpitz and a boreal site at Hyytiälä in Finland (Zieger et al., 2014, 2015); all showed good overlap with those from ACE-Asia and ORACLES. The linear regression for ORACLES, $\gamma = (1.16 \pm 0.02) - (1.11 \pm 0.02) \cdot F_O$, retrieved from an orthogonal fit by taking the standard deviation as the input for uncertainty calculation, is very similar to those in Hyytiälä and ACE-Asia, though the slope is slightly lower.

We explored the γ–F_O relationship with the Mie model and found that the relationship observed can be largely explained by aerosol chemical composition and OA hygroscopicity. The γ values were calculated with the scattering coefficients simulated in both dry conditions and at 80 % RH. Simulations were performed with the Mie model for internally mixed OA–$(NH_4)_2SO_4$–BC mixtures with an assumed BC mass ratio (BCr, 5 % and 25 %) and κ_{OA} values (0–0.6), which encompass the ranges observed in ORACLES (refer to Sect. 3.2 for κ_{OA} values). The PNSD was assumed to be lognormally distributed, with a geometric mean diameter (D_{gn}) of 150 nm and a standard deviation (σ_{sg}) of 1.6. As shown in Fig. 6 (solid and dashed purple, green, and blue lines), simulated curves can capture most of the observations. F_O and κ_{OA} dominate γ, and BC shows a small negative impact. It is noteworthy that the (negative) slope of the γ–F_O relationship increases with increasing κ_{OA} up to κ_{OA} values of 0.6, where γ exhibits little variation with F_O. Therefore, we conclude that the variation of BBA hygroscopicity with aging in the SEA is mainly due to changes in chemical composition, particularly sulfate and OA, as well as the variation of OA hygroscopicity during transport. The higher BC fraction in aged aerosols compared to less-aged ones has slightly decreased the hygroscopicity of aged aerosols.

3.3.2 Parameterization of γ using Mie simulations of internally mixed OA–$(NH_4)_2SO_4$–BC mixtures

Mie simulations are performed for internally mixed OA–$(NH_4)_2SO_4$–BC mixtures to obtain the scattering coefficient of dry and humidified aerosols. We assume PNSD to be a lognormal distribution with $D_{gn} = 150$ nm and $\sigma_{sg} = 1.6$, like the approximation of D_{gn} and σ_{sg} in the ORACLES 2016 and 2018 campaigns. The RH and RH_{ref} are set as 80 % and 0, respectively. The γ is then calculated following Eq. (2). The F_O, κ_{OA}, and BCr are varied from 0 to 1, 0 to 0.9, and 0 to 1, respectively, all in increments of 0.02. Taking $\gamma(F_O, \kappa_{OA} = 0, \text{BCr})$ as the baseline (refer to solid and dashed blue lines in Fig. 6), we calculated the product $M(F_O, \kappa_{OA}, \text{BCr})$ of $\gamma(F_O, \kappa_{OA} = 0, \text{BCr})$ and $\gamma(F_O, \kappa_{OA}, \text{BCr})$ for each κ_{OA} and BCr, i.e., $M(F_O, \kappa_{OA}, \text{BCr}) = \gamma(F_O, \kappa_{OA} = 0, \text{BCr}) \times \gamma(F_O, \kappa_{OA}, \text{BCr})$, and found that the relationship between $M(F_O, \kappa_{OA}, \text{BCr})$ and F_O can be fitted well into a quadratic (second-order) polynomial function, i.e., $M(F_O, \kappa_{OA}, \text{BCr}) = aF_O^2 + bF_O + c$ (Fig. 7a). The variation of $M(F_O, \kappa_{OA}, \text{BCr})$ with F_O and the R^2 of the regression are shown in Fig. 7a and e, respectively. The fitted coefficients a, b, and c, as shown in Fig. 7b, c, and d, coincidentally fit well as quadratic functions of κ_{OA}, whose coefficients, in turn, can be fitted well into a fifth-order polynomial function of BCr. Results are shown in Fig. S3 in the Supplement. In sum, the $M(F_O, \kappa_{OA}, \text{BCr})$ can be parameterized as follows.

$$M(F_O, \kappa_{OA}, \text{BCr}) = \sum_{\substack{i \le 2 \\ j \le 2 \\ k \le 5}} a_{ijk} \text{BCr}^k \kappa_{OA}^j F_O^i \quad (4)$$

Similarly, $\gamma(F_O, \kappa_{OA} = 0, \text{BCr})$ can be fitted well into a quadratic function of F_O with coefficients that fit well with a fifth-order polynomial function of BCr.

$$\gamma(F_O, \kappa_{OA} = 0, \text{BCr}) = \sum_{\substack{i \le 2 \\ k \le 5}} a_{ik} \text{BCr}^k F_O^i \quad (5)$$

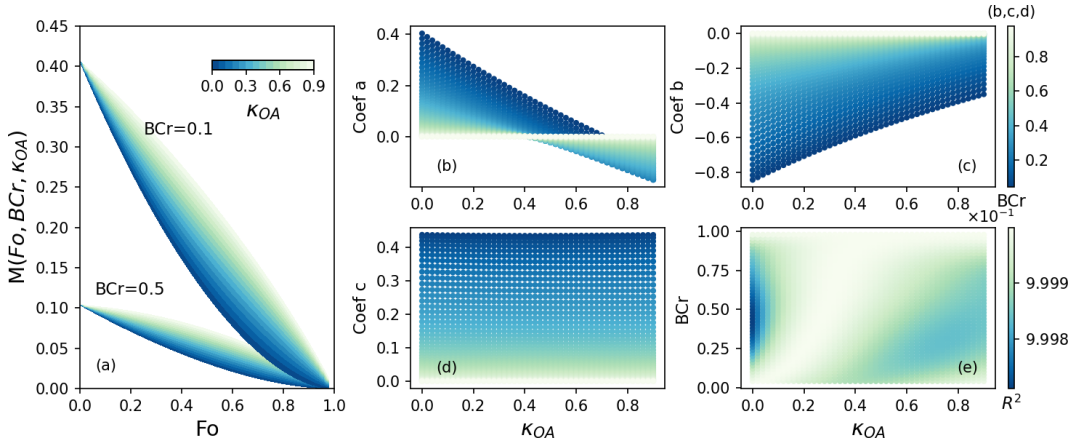

Figure 7. **(a)** Variations of $M(F_O, \kappa_{OA}, BCr)$ with F_O colored by κ_{OA} at BCr of 0.1 and 0.5 for internally mixed OA–$(NH_4)_2SO_4$–BC mixtures. $M(F_O, \kappa_{OA}, BCr)$ is the product of $\gamma(F_O, \kappa_{OA} = 0, BCr)$ and $\gamma(F_O, \kappa_{OA}, BCr)$ for each κ_{OA} value. F_O represents the ratio of the mass concentration of OA to that of OA and SO_4^{2-}. BCr is the mass ratio of BC. **(b, c, d)** Variation of coefficients a, b, and c with κ_{OA} and BCr. The coefficients a, b, and c are the fitted parameters of the quadratic regression between $M(F_O, \kappa_{OA}, BCr)$ and F_O for each κ_{OA} and BCr. **(e)** The R^2 (color bar) of the $M(F_O, \kappa_{OA}, BCr)$ regression with F_O as a function of κ_{OA} and BCr.

Equations (4) and (5) in matrix format are referred to as Eqs. (S1) and (S2) in the Supplement, respectively. Values of coefficients a_{ijk} and a_{ik} are shown in Table S3. Therefore, $\gamma(F_O, \kappa_{OA}, BCr)$ can be calculated as the ratio of $M(F_O, \kappa_{OA}, BCr)$ to $\gamma(F_O, \kappa_{OA} = 0, BCr)$.

$$\gamma(F_O, \kappa_{OA}, BCr) = \frac{M(F_O, \kappa_{OA}, BCr)}{\gamma(F_O, \kappa_{OA} = 0, BCr)} \quad (6)$$

We evaluated this parameterization by comparing the predicted and measured $f(80\,\%)$ for the ORACLES 2016 and 2018 campaigns. The predicted $f(80\,\%)$ is calculated with Eq. (6) with F_O, κ_{OA}, and BCr as inputs and Eq. (2) with the dry and humidified RHs measured in both campaigns. Note that the mean BC mass ratio for each year has been used in the calculation, as little difference has been observed using the temporal BCr and mean BCr. Good correlation of measured and predicted $f(80\,\%)$ has been achieved for both years' campaigns, as shown in Fig. 8a. This indicates that the internally mixed OA–$(NH_4)_2SO_4$–BC mixture with PNSD ($D_{gn} = 150$ nm and $\sigma_{sg} = 1.6$) is a good approximation of aerosols with respect to the $f(RH)$ prediction for the 2016 and 2018 ORACLES campaigns. The influence of PNSD on $f(RH)$ is small and discussed in Sect. S1 in the Supplement.

3.3.3 Sensitivity of aerosol scattering enhancement to κ_{OA}

Due to the chemical complexity of OA, the κ_{OA} values of particles are not easily obtained. Various hygroscopicity parameterizations have been proposed in previous studies, most of which are parameterized with chemical composition, e.g., organic or inorganic fraction, and a constant assumed κ_{OA} value. Few studies consider the variation of κ_{OA} (Zhang et al., 2015; Huang et al., 2022). While these parameterizations can represent their observations well, they may not be suitable for situations with different κ_{OA} values. Therefore, in this section, the influence of κ_{OA} on the prediction of $f(RH)$ is analyzed. We calculated the $f(80\,\%)$ with the mean κ_{OA} in each campaign, and the results are shown in Fig. 8b. The use of a constant κ_{OA} average leads to a much smaller variation of the predicted $f(80\,\%)$ values, most of which is concentrated around 1.3–1.4. Predicted $f(80\,\%)$ tends to overestimate lower $f(80\,\%)$ values while underestimating higher $f(80\,\%)$ values. A slope of 0.50 and R^2 of 0.01 indicate poor prediction in capturing the trend of $f(80\,\%)$. This indicates that using F_O, BCr, and a constant κ_{OA} is insufficient for the prediction of $f(RH)$ and that the variation of κ_{OA} needs to be considered, at least for situations where κ_{OA} has a large variation, such as in ORACLES.

To quantitatively investigate the sensitivity of $f(RH)$ to κ_{OA}, we calculated the deviation of $f(80\,\%)$ with κ_{OA} for the OA–$(NH_4)_2SO_4$–BC mixture. The deviation of $f(80\,\%)$ was calculated as $f(80\,\%, \kappa_{OA}) - f(80\,\%, \kappa_{OA} = 0)$. As shown in Fig. 9, we observed that κ_{OA} is positively correlated with $f(80\,\%)$. Additionally, the deviation of $f(80\,\%)$ is dependent on the OA fraction (F_O); i.e., a higher OA fraction leads to a larger impact of κ_{OA} and consequently a larger deviation of $f(80\,\%)$.

The 25th and 75th percentiles of F_O for the 2016 and 2018 ORACLES campaigns were 0.74 and 0.86, respectively. These are relatively high values and therefore result in a relatively high spread of $f(80\,\%)$. Additionally, the age of ORACLES OA spans from < 4 to > 10 d, during which OA oxidation and fragmentation (as discussed in Sect. 3.2) take place. These processes alter the hygroscopicity of OA, causing the OA in ORACLES to contribute to large variations of κ_{OA}. These large variations of κ_{OA}, combined with the rela-

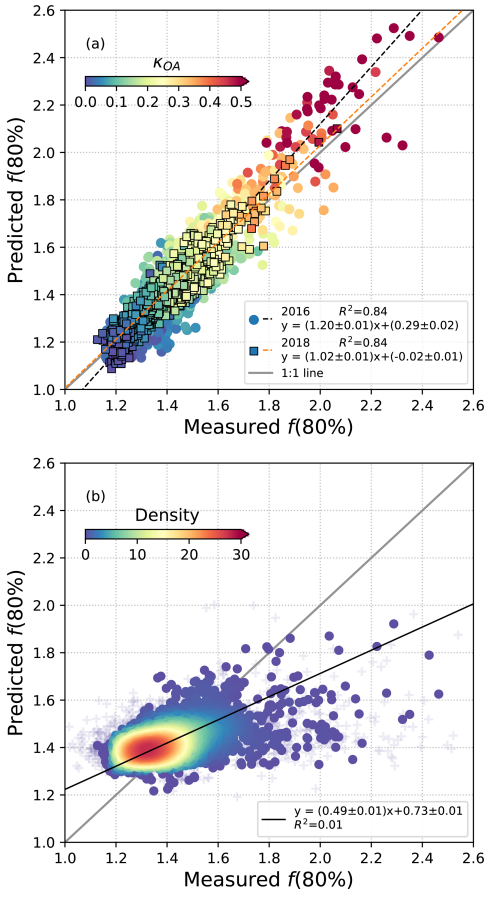

Figure 8. Measured $f(80\,\%)$ vs. predicted $f(80\,\%)$ using the γ parameterization for internally mixed OA–$(NH_4)_2SO_4$–BC mixtures. The $f(80\,\%)$ in panel **(a)** is calculated with κ_{OA} values colored by κ_{OA}, and in panel **(b)** it is predicted with the mean κ_{OA} values. Dashed black and orange lines in panel **(a)** represent the ordinary linear regression for 2016 and 2018, respectively. The dashed black line in panel **(b)** represents the ordinary linear regression for the two years. The solid gray line is the 1 : 1 line.

tively high OA fraction (F_O), make $f(RH)$ highly sensitive to the κ_{OA} value. For aerosols with a κ_{OA} of 0.4 and F_O of 0.86, the $f(80\,\%)$ can be 80 % higher compared to aerosols with hydrophobic OA, as shown in Fig. 9. In other words, the aerosol scattering coefficients at 80 % RH are 80 % higher solely because of the increase in OA hygroscopicity. This high sensitivity also explains the poor prediction of $f(80\,\%)$ when using campaign mean κ_{OA} values, as shown in Fig. 8b. Many studies overlook the variability of κ_{OA} and instead use a constant κ_{OA} when analyzing aerosol hygroscopicity or radiative forcing. As illustrated in Fig. 9, this can be reasonable when the OA fraction is low and κ_{OA} exhibits minimal variation; however, in cases where these two conditions are not met, κ_{OA} can significantly influence the scattering coefficients and hence direct radiative forcing.

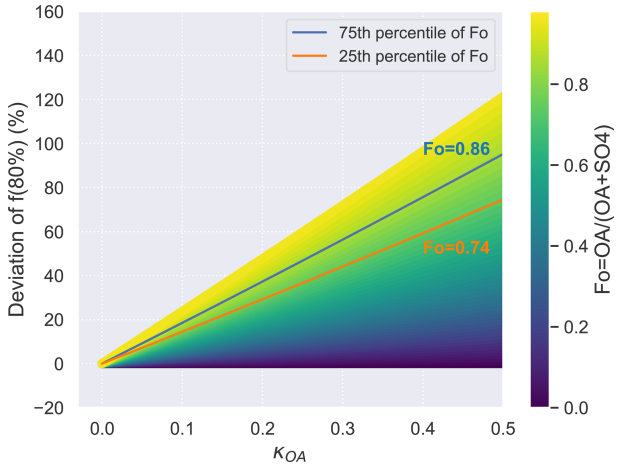

Figure 9. Sensitivity of the deviation of $f(80\,\%)$ to κ_{OA}. The deviation of $f(80\,\%)$ was calculated as $f(80\,\%, \kappa_{OA}) - f(80\,\%, \kappa_{OA} = 0)$. The OA to $OA + SO_4$ ratio (F_O) is represented by the color bar. The blue and orange lines represent the variation in the 75th and 25th percentiles of F_O in both years' ORACLES campaigns, respectively.

4 Conclusion

The hygroscopicity of aerosols from the perspective of scattering enhancement over the SEA Ocean during the BB season is investigated using measurements from the 2016 and 2018 ORACLES campaigns. The vertical distribution of aerosol hygroscopicity shows a consistent pattern in both campaigns, remaining stable above 2 km; below 2 km, aerosols are more hygroscopic at lower altitudes. Aerosols above 2 km have a mean and standard deviation for $f(80\,\%)$ and $\kappa_{f(RH)}$ of 1.40 ± 0.17 and 0.19 ± 0.07, respectively, and are less hygroscopic. Conversely, aerosols below 2 km are more hygroscopic and have a mean and standard deviation for $f(80\,\%)$ and $\kappa_{f(RH)}$ of 1.51 ± 0.22 and 0.23 ± 0.08, respectively, which are values in the upper range of BBA hygroscopicity found in the literature. This variation of aerosol hygroscopicity is consistent with the vertical variation of chemical composition. The OA and sulfate mass fractions in both years show little variation above 2 km; below this altitude, OA decreases with decreasing altitude, while the sulfate mass fraction tends to increase. OA oxidation through molecular fragmentation is the main mechanism for OA losses in the FT, while the increase in sulfate in the MBL could indicate a marine influence.

We retrieved κ_{OA} using Mie simulations. It shows a large variation, with the mean and standard deviation being 0.11 ± 0.08 and with 25th and 75th percentiles of 0.06 and 0.16, respectively. No clear relationship was found between κ_{OA} and OA oxidation level, while a slight increase in κ_{OA} with volatility is shown in 2016, which may be related to the fragmentation during OA oxidation, where the highly aged and low-volatility OA may dissociate into more volatile frag-

ments that are still highly functionalized and hygroscopic. Overall, OA hygroscopicity under subsaturated conditions can be largely influenced by solubility, molecular weight, molecular functional groups, and carbon number (Cai et al., 2021; Kuang et al., 2020a; Rastak et al., 2017; Rickards et al., 2013; Suda et al., 2012); to better understand the variation of κ_{OA}, more molecular investigations are needed.

In comparison with other campaigns, we find that the variation of aerosol hygroscopicity in the SEA is mainly due to changes in chemical composition, particularly sulfate and OA, as well as variations in OA hygroscopicity during transport. To quantitatively investigate this relationship, we came up with a parameterization using F_O, BCr, and κ_{OA}, as well as the $f(80\,\%)$ from Mie simulations for an internally mixed OA–$(NH_4)_2SO_4$–BC mixture with PNSD ($D_{gn} = 150$ nm and $\sigma_{sg} = 1.6$). This suggests that the internal mixture of OA–$(NH_4)_2SO_4$–BC is a good approximation of aerosols with respect to the $f(RH)$ prediction for the 2016 and 2018 ORACLES campaigns.

A sensitivity study indicates that solely due to the increase in OA hygroscopicity observed in our study, the aerosol scattering coefficients at 80 % RH can be amplified by 80 %. Relying on the campaign mean κ_{OA} value leads to a poor prediction of $f(80\,\%)$. The dependence of $f(RH)$ on κ_{OA} suggests that using a constant κ_{OA} can be acceptable when the OA fraction is low and κ_{OA} demonstrates limited variations. However, in situations where these two conditions are not met, κ_{OA} can significantly influence the scattering coefficients and thus aerosol radiative effect. Therefore, accommodating the variability of κ_{OA} is advisable.

Data availability. Datasets are publicly available via the digital object identifier provided under the ORACLES Science Team reference: https://doi.org/10.5067/Suborbital/ORACLES/P3/2018_V2 (ORACLES Science Team, 2020).

Supplement. The supplement related to this article is available online at: https://doi.org/10.5194/acp-24-13849-2024-supplement.

Author contributions. LZ, MSR, and HC designed the research. MSR conducted the measurements. LZ, HC, and CD analyzed the data, with all co-authors advancing the overall analysis further. LZ wrote the paper with support from all co-authors.

Competing interests. At least one of the (co-)authors is a guest member of the editorial board of *Atmospheric Chemistry and Physics* for the special issue "New observations and related modelling studies of the aerosol–cloud–climate system in the Southeast Atlantic and southern Africa regions (ACP/AMT inter-journal SI)". The peer-review process was guided by an independent editor, and the authors also have no other competing interests to declare.

Disclaimer. Publisher's note: Copernicus Publications remains neutral with regard to jurisdictional claims made in the text, published maps, institutional affiliations, or any other geographical representation in this paper. While Copernicus Publications makes every effort to include appropriate place names, the final responsibility lies with the authors.

Special issue statement. This article is part of the special issue "New observations and related modelling studies of the aerosol–cloud–climate system in the Southeast Atlantic and southern Africa regions (ACP/AMT inter-journal SI)". It is not associated with a conference.

Acknowledgements. The authors would like to thank the ORACLES team. Lu Zhang is grateful for the postdoctoral fellowship funding from the Tel Aviv University Department of Exact Sciences. Caroline Dang is grateful for the NASA postdoctoral fellowship grant. The authors thank Paul Zieger for useful comments on this article.

Financial support. This research has been supported by the United States Department of Energy Atmospheric System Research (ASR; grant DE-SC0020084); the AErosols, RadiatiOn and CLOuds in southern Africa (AEROCLO-sA) project funded by the French National Research Agency (grant agreement no. ANR-15-CE01-0014-01); the French national programs LEFE/INSU and PNTS; the French National Agency for Space Studies (CNES); the European Union's Seventh Framework Programme (FP7/2014–2018; EUFAR2 contract no. 312609); and the South African National Research Foundation (NRF; grant UID 105958).

Review statement. This paper was edited by Birgit Wehner and reviewed by three anonymous referees.

References

Alexander, B., Park, R. J., Jacob, D. J., Li, Q. B., Yantosca, R. M., Savarino, J., Lee, C. C. W., and Thiemens, M. H.: Sulfate formation in sea-salt aerosols: Constraints from oxygen isotopes, J. Geophys. Res.-Atmos., 110, D10307, https://doi.org/10.1029/2004JD005659, 2005.

Anderson, T. L. and Ogren, J. A.: Determining Aerosol Radiative Properties Using the TSI 3563 Integrating Nephelometer, Aerosol Sci. Tech., 29, 57–69, https://doi.org/10.1080/02786829808965551, 1998.

Andreae, M. O., Elbert, W., and de Mora, S. J.: Biogenic sulfur emissions and aerosols over the tropical South Atlantic: 3. Atmospheric dimethylsulfide, aerosols and cloud condensation nuclei, J. Geophys. Res.-Atmos., 100, 11335–11356, https://doi.org/10.1029/94JD02828, 1995.

Asa-Awuku, A., Sullivan, A. P., Hennigan, C. J., Weber, R. J., and Nenes, A.: Investigation of molar volume and surfactant characteristics of water-soluble organic compounds in

biomass burning aerosol, Atmos. Chem. Phys., 8, 799–812, https://doi.org/10.5194/acp-8-799-2008, 2008.

Bukowiecki, N., Weingartner, E., Gysel, M., Coen, M. C., Zieger, P., Herrmann, E., Steinbacher, M., Gäggeler, H. W., and Baltensperger, U.: A Review of More than 20 Years of Aerosol Observation at the High Altitude Research Station Jungfraujoch, Switzerland (3580 m a.s.l.), Aerosol Air Qual. Res., 16, 764–788, https://doi.org/10.4209/aaqr.2015.05.0305, 2016.

Burgos, M. A., Andrews, E., Titos, G., Benedetti, A., Bian, H., Buchard, V., Curci, G., Kipling, Z., Kirkevåg, A., Kokkola, H., Laakso, A., Letertre-Danczak, J., Lund, M. T., Matsui, H., Myhre, G., Randles, C., Schulz, M., van Noije, T., Zhang, K., Alados-Arboledas, L., Baltensperger, U., Jefferson, A., Sherman, J., Sun, J., Weingartner, E., and Zieger, P.: A global model–measurement evaluation of particle light scattering coefficients at elevated relative humidity, Atmos. Chem. Phys., 20, 10231–10258, https://doi.org/10.5194/acp-20-10231-2020, 2020.

Cai, M., Liang, B., Sun, Q., Liu, L., Yuan, B., Shao, M., Huang, S., Peng, Y., Wang, Z., Tan, H., Li, F., Xu, H., Chen, D., and Zhao, J.: The important roles of surface tension and growth rate in the contribution of new particle formation (NPF) to cloud condensation nuclei (CCN) number concentration: evidence from field measurements in southern China, Atmos. Chem. Phys., 21, 8575–8592, https://doi.org/10.5194/acp-21-8575-2021, 2021.

Carrico, C. M., Kus, P., Rood, M. J., Quinn, P. K., and Bates, T. S.: Mixtures of pollution, dust, sea salt, and volcanic aerosol during ACE-Asia: Radiative properties as a function of relative humidity, J. Geophys. Res.-Atmos., 108, 8650, https://doi.org/10.1029/2003JD003405, 2003.

Cerully, K. M., Bougiatioti, A., Hite Jr., J. R., Guo, H., Xu, L., Ng, N. L., Weber, R., and Nenes, A.: On the link between hygroscopicity, volatility, and oxidation state of ambient and water-soluble aerosols in the southeastern United States, Atmos. Chem. Phys., 15, 8679–8694, https://doi.org/10.5194/acp-15-8679-2015, 2015.

Che, H., Zhang, X., Zhang, L., Wang, Y., Zhang, Y., Shen, X., Ma, Q., Sun, J., and Zhong, J.: Prediction of size-resolved number concentration of cloud condensation nuclei and long-term measurements of their activation characteristics, Sci. Rep., 7, 5819, https://doi.org/10.1038/s41598-017-05998-3, 2017.

Che, H., Segal-Rozenhaimer, M., Zhang, L., Dang, C., Zuidema, P., Dobracki, A., Sedlacek, A. J., Coe, H., Wu, H., Taylor, J., Zhang, X., Redemann, J., and Haywood, J.: Cloud processing and weeklong ageing affect biomass burning aerosol properties over the south-eastern Atlantic, Commun. Earth Environ., 3, 182, https://doi.org/10.1038/s43247-022-00517-3, 2022a.

Che, H., Stier, P., Watson-Parris, D., Gordon, H., and Deaconu, L.: Source attribution of cloud condensation nuclei and their impact on stratocumulus clouds and radiation in the south-eastern Atlantic, Atmos. Chem. Phys., 22, 10789–10807, https://doi.org/10.5194/acp-22-10789-2022, 2022b.

Che, H., Segal-Rozenhaimer, M., Zhang, L., Dang, C., Zuidema, P., Sedlacek III, A. J., Zhang, X., and Flynn, C.: Seasonal variations in fire conditions are important drivers in the trend of aerosol optical properties over the south-eastern Atlantic, Atmos. Chem. Phys., 22, 8767–8785, https://doi.org/10.5194/acp-22-8767-2022, 2022c.

Chen, J., Zhao, C. S., Ma, N., and Yan, P.: Aerosol hygroscopicity parameter derived from the light scattering enhancement factor measurements in the North China Plain, Atmos. Chem. Phys., 14, 8105–8118, https://doi.org/10.5194/acp-14-8105-2014, 2014.

Cotterell, M. I., Willoughby, R. E., Bzdek, B. R., Orr-Ewing, A. J., and Reid, J. P.: A complete parameterisation of the relative humidity and wavelength dependence of the refractive index of hygroscopic inorganic aerosol particles, Atmos. Chem. Phys., 17, 9837–9851, https://doi.org/10.5194/acp-17-9837-2017, 2017.

Covert, D. S., Charlson, R. J., and Ahlquist, N. C.: A Study of the Relationship of Chemical Composition and Humidity to Light Scattering by Aerosols, J. Appl. Meteorol., 11, 968–976, https://doi.org/10.1175/1520-0450(1972)011<0968:ASOTRO>2.0.CO;2, 1972.

Cubison, M. J., Ortega, A. M., Hayes, P. L., Farmer, D. K., Day, D., Lechner, M. J., Brune, W. H., Apel, E., Diskin, G. S., Fisher, J. A., Fuelberg, H. E., Hecobian, A., Knapp, D. J., Mikoviny, T., Riemer, D., Sachse, G. W., Sessions, W., Weber, R. J., Weinheimer, A. J., Wisthaler, A., and Jimenez, J. L.: Effects of aging on organic aerosol from open biomass burning smoke in aircraft and laboratory studies, Atmos. Chem. Phys., 11, 12049–12064, https://doi.org/10.5194/acp-11-12049-2011, 2011.

Dang, C., Segal-Rozenhaimer, M., Che, H., Zhang, L., Formenti, P., Taylor, J., Dobracki, A., Purdue, S., Wong, P.-S., Nenes, A., Sedlacek III, A., Coe, H., Redemann, J., Zuidema, P., Howell, S., and Haywood, J.: Biomass burning and marine aerosol processing over the southeast Atlantic Ocean: a TEM single-particle analysis, Atmos. Chem. Phys., 22, 9389–9412, https://doi.org/10.5194/acp-22-9389-2022, 2022.

Day, D. E., Hand, J. L., Carrico, C. M., Engling, G., and Malm, W. C.: Humidification factors from laboratory studies of fresh smoke from biomass fuels, J. Geophys. Res.-Atmos., 111, D22202, https://doi.org/10.1029/2006JD007221, 2006.

DeCarlo, P. F., Slowik, J. G., Worsnop, D. R., Davidovits, P., and Jimenez, J. L.: Particle Morphology and Density Characterization by Combined Mobility and Aerodynamic Diameter Measurements. Part 1: Theory, Aerosol Sci. Tech., 38, 1185–1205, https://doi.org/10.1080/027868290903907, 2004.

Dobracki, A., Zuidema, P., Howell, S. G., Saide, P., Freitag, S., Aiken, A. C., Burton, S. P., Sedlacek III, A. J., Redemann, J., and Wood, R.: An attribution of the low single-scattering albedo of biomass burning aerosol over the southeastern Atlantic, Atmos. Chem. Phys., 23, 4775–4799, https://doi.org/10.5194/acp-23-4775-2023, 2023.

Donahue, N. M., Kroll, J. H., Pandis, S. N., and Robinson, A. L.: A two-dimensional volatility basis set – Part 2: Diagnostics of organic-aerosol evolution, Atmos. Chem. Phys., 12, 615–634, https://doi.org/10.5194/acp-12-615-2012, 2012.

Ervens, B., Cubison, M., Andrews, E., Feingold, G., Ogren, J. A., Jimenez, J. L., DeCarlo, P., and Nenes, A.: Prediction of cloud condensation nucleus number concentration using measurements of aerosol size distributions and composition and light scattering enhancement due to humidity, J. Geophys. Res.-Atmos., 112, D10S32, https://doi.org/10.1029/2006JD007426, 2007.

Gras, J. L., Jensen, J. B., Okada, K., Ikegami, M., Zaizen, Y., and Makino, Y.: Some optical properties of smoke aerosol in Indonesia and tropical Australia, Geophys. Res. Lett., 26, 1393–1396, https://doi.org/10.1029/1999GL900275, 1999.

Gysel, M., Crosier, J., Topping, D. O., Whitehead, J. D., Bower, K. N., Cubison, M. J., Williams, P. I., Flynn, M. J., McFiggans, G. B., and Coe, H.: Closure study between chemical composition

and hygroscopic growth of aerosol particles during TORCH2, Atmos. Chem. Phys., 7, 6131–6144, https://doi.org/10.5194/acp-7-6131-2007, 2007.

Haywood, J., Bush, M., Abel, S., Claxton, B., Coe, H., Crosier, J., Harrison, M., Macpherson, B., Naylor, M., and Osborne, S.: Prediction of visibility and aerosol within the operational Met Office Unified Model. II: Validation of model performance using observational data, Q. J. Roy. Meteor. Soc., 134, 1817–1832, https://doi.org/10.1002/qj.275, 2008.

Howell, S. G., Clarke, A. D., Shinozuka, Y., Kapustin, V., McNaughton, C. S., Huebert, B. J., Doherty, S. J., and Anderson, T. L.: Influence of relative humidity upon pollution and dust during ACE-Asia: Size distributions and implications for optical properties, J. Geophys. Res., 111, 2004JD005759, https://doi.org/10.1029/2004JD005759, 2006.

Howell, S. G., Freitag, S., Dobracki, A., Smirnow, N., and Sedlacek III, A. J.: Undersizing of aged African biomass burning aerosol by an ultra-high-sensitivity aerosol spectrometer, Atmos. Meas. Tech., 14, 7381–7404, https://doi.org/10.5194/amt-14-7381-2021, 2021.

Huang, S., Wu, Z., Wang, Y., Poulain, L., Höpner, F., Merkel, M., Herrmann, H., and Wiedensohler, A.: Aerosol Hygroscopicity and its Link to Chemical Composition in a Remote Marine Environment Based on Three Transatlantic Measurements, Environ. Sci. Technol., 56, 9613–9622, https://doi.org/10.1021/acs.est.2c00785, 2022.

Kacarab, M., Thornhill, K. L., Dobracki, A., Howell, S. G., O'Brien, J. R., Freitag, S., Poellot, M. R., Wood, R., Zuidema, P., Redemann, J., and Nenes, A.: Biomass burning aerosol as a modulator of the droplet number in the southeast Atlantic region, Atmos. Chem. Phys., 20, 3029–3040, https://doi.org/10.5194/acp-20-3029-2020, 2020.

Kim, J., Yoon, S.-C., Jefferson, A., and Kim, S.-W.: Aerosol hygroscopic properties during Asian dust, pollution, and biomass burning episodes at Gosan, Korea in April 2001, Atmos. Environ., 40, 1550–1560, https://doi.org/10.1016/j.atmosenv.2005.10.044, 2006.

Klopper, D., Formenti, P., Namwoonde, A., Cazaunau, M., Chevaillier, S., Feron, A., Gaimoz, C., Hease, P., Lahmidi, F., Mirande-Bret, C., Triquet, S., Zeng, Z., and Piketh, S. J.: Chemical composition and source apportionment of atmospheric aerosols on the Namibian coast, Atmos. Chem. Phys., 20, 15811–15833, https://doi.org/10.5194/acp-20-15811-2020, 2020.

Kotchenruther, R. A. and Hobbs, P. V.: Humidification factors of aerosols from biomass burning in Brazil, J. Geophys. Res.-Atmos., 103, 32081–32089, https://doi.org/10.1029/98JD00340, 1998.

Kroll, J. H., Donahue, N. M., Jimenez, J. L., Kessler, S. H., Canagaratna, M. R., Wilson, K. R., Altieri, K. E., Mazzoleni, L. R., Wozniak, A. S., Bluhm, H., Mysak, E. R., Smith, J. D., Kolb, C. E., and Worsnop, D. R.: Carbon oxidation state as a metric for describing the chemistry of atmospheric organic aerosol, Nat. Chem., 3, 133–139, https://doi.org/10.1038/nchem.948, 2011.

Kuang, Y., Xu, W., Tao, J., Ma, N., Zhao, C., and Shao, M.: A Review on Laboratory Studies and Field Measurements of Atmospheric Organic Aerosol Hygroscopicity and Its Parameterization Based on Oxidation Levels, Curr. Pollut. Rep., 6, 410–424, https://doi.org/10.1007/s40726-020-00164-2, 2020a.

Kuang, Y., He, Y., Xu, W., Zhao, P., Cheng, Y., Zhao, G., Tao, J., Ma, N., Su, H., Zhang, Y., Sun, J., Cheng, P., Yang, W., Zhang, S., Wu, C., Sun, Y., and Zhao, C.: Distinct diurnal variation in organic aerosol hygroscopicity and its relationship with oxygenated organic aerosol, Atmos. Chem. Phys., 20, 865–880, https://doi.org/10.5194/acp-20-865-2020, 2020b.

Kuang, Y., Huang, S., Xue, B., Luo, B., Song, Q., Chen, W., Hu, W., Li, W., Zhao, P., Cai, M., Peng, Y., Qi, J., Li, T., Wang, S., Chen, D., Yue, D., Yuan, B., and Shao, M.: Contrasting effects of secondary organic aerosol formations on organic aerosol hygroscopicity, Atmos. Chem. Phys., 21, 10375–10391, https://doi.org/10.5194/acp-21-10375-2021, 2021.

Lambe, A. T., Onasch, T. B., Massoli, P., Croasdale, D. R., Wright, J. P., Ahern, A. T., Williams, L. R., Worsnop, D. R., Brune, W. H., and Davidovits, P.: Laboratory studies of the chemical composition and cloud condensation nuclei (CCN) activity of secondary organic aerosol (SOA) and oxidized primary organic aerosol (OPOA), Atmos. Chem. Phys., 11, 8913–8928, https://doi.org/10.5194/acp-11-8913-2011, 2011.

Liu, P., Song, M., Zhao, T., Gunthe, S. S., Ham, S., He, Y., Qin, Y. M., Gong, Z., Amorim, J. C., Bertram, A. K., and Martin, S. T.: Resolving the mechanisms of hygroscopic growth and cloud condensation nuclei activity for organic particulate matter, Nat. Commun., 9, 1–10, https://doi.org/10.1038/s41467-018-06622-2, 2018.

Liu, P. F., Zhao, C. S., Göbel, T., Hallbauer, E., Nowak, A., Ran, L., Xu, W. Y., Deng, Z. Z., Ma, N., Mildenberger, K., Henning, S., Stratmann, F., and Wiedensohler, A.: Hygroscopic properties of aerosol particles at high relative humidity and their diurnal variations in the North China Plain, Atmos. Chem. Phys., 11, 3479–3494, https://doi.org/10.5194/acp-11-3479-2011, 2011.

Liu, X. and Wang, J.: How important is organic aerosol hygroscopicity to aerosol indirect forcing?, Environ. Res. Lett., 5, 044010, https://doi.org/10.1088/1748-9326/5/4/044010, 2010.

Magi, B. I. and Hobbs, P. V.: Effects of humidity on aerosols in southern Africa during the biomass burning season, J. Geophys. Res.-Atmos., 108, 8495, https://doi.org/10.1029/2002JD002144, 2003.

Mayer, K. J., Wang, X., Santander, M. V., Mitts, B. A., Sauer, J. S., Sultana, C. M., Cappa, C. D., and Prather, K. A.: Secondary Marine Aerosol Plays a Dominant Role over Primary Sea Spray Aerosol in Cloud Formation, ACS Cent. Sci., 6, 2259–2266, https://doi.org/10.1021/acscentsci.0c00793, 2020.

McNaughton, C. S., Clarke, A. D., Howell, S. G., Pinkerton, M., Anderson, B., Thornhill, L., Hudgins, C., Winstead, E., Dibb, J. E., Scheuer, E., and Maring, H.: Results from the DC-8 Inlet Characterization Experiment (DICE): Airborne Versus Surface Sampling of Mineral Dust and Sea Salt Aerosols, Aerosol Sci. Tech., 41, 136–159, https://doi.org/10.1080/02786820601118406, 2007.

Mei, F., Hayes, P. L., Ortega, A., Taylor, J. W., Allan, J. D., Gilman, J., Kuster, W., de Gouw, J., Jimenez, J. L., and Wang, J.: Droplet activation properties of organic aerosols observed at an urban site during CalNex-LA, J. Geophys. Res.-Atmos., 118, 2903–2917, https://doi.org/10.1002/jgrd.50285, 2013.

Mie, G.: Beiträge zur Optik trüber Medien, speziell kolloidaler Metallösungen, Ann. Phys., 330, 377–445, https://doi.org/10.1002/andp.19083300302, 1908.

NASA/LARC/SD/ASDC: DISCOVER-AQ Colorado Deployment Ancillary Model Data, NASA Langley Atmospheric Science Data Center DAAC [data set], https://doi.org/10.5067/ASDC/SUBORBITAL/DISCOVERAQ_Colorado_Model_Data_1, 2022.

Ng, N. L., Canagaratna, M. R., Jimenez, J. L., Chhabra, P. S., Seinfeld, J. H., and Worsnop, D. R.: Changes in organic aerosol composition with aging inferred from aerosol mass spectra, Atmos. Chem. Phys., 11, 6465–6474, https://doi.org/10.5194/acp-11-6465-2011, 2011.

ORACLES Science Team: Suite of Aerosol, Cloud, and Related Data Acquired Aboard P3 During ORACLES 2018, Version 2, Observations of Aerosols Above Clouds and Their Interactions (ORACLES), NASA Ames Earth Science Project Office (ESPO), Moffett Field, CA [data set], https://doi.org/10.5067/Suborbital/ORACLES/P3/2018_V2, 2020.

Petters, M. D. and Kreidenweis, S. M.: A single parameter representation of hygroscopic growth and cloud condensation nucleus activity, Atmos. Chem. Phys., 7, 1961–1971, https://doi.org/10.5194/acp-7-1961-2007, 2007.

Petters, M. D., Carrico, C. M., Kreidenweis, S. M., Prenni, A. J., DeMott, P. J., Collett, J. L., and Moosmüller, H.: Cloud condensation nucleation activity of biomass burning aerosol, J. Geophys. Res., 114, D22205, https://doi.org/10.1029/2009JD012353, 2009.

Quinn, P. K., Bates, T. S., Baynard, T., Clarke, A. D., Onasch, T. B., Wang, W., Rood, M. J., Andrews, E., Allan, J., Carrico, C. M., Coffman, D., and Worsnop, D.: Impact of particulate organic matter on the relative humidity dependence of light scattering: A simplified parameterization, Geophys. Res. Lett., 32, L22809, https://doi.org/10.1029/2005GL024322, 2005.

Ramo, R., Roteta, E., Bistinas, I., van Wees, D., Bastarrika, A., Chuvieco, E., and van der Werf, G. R.: African burned area and fire carbon emissions are strongly impacted by small fires undetected by coarse resolution satellite data, P. Natl. Acad. Sci. USA, 118, e2011160118, https://doi.org/10.1073/pnas.2011160118, 2021.

Rastak, N., Pajunoja, A., Acosta Navarro, J. C., Ma, J., Song, M., Partridge, D. G., Kirkevåg, A., Leong, Y., Hu, W. W., Taylor, N. F., Lambe, A., Cerully, K., Bougiatioti, A., Liu, P., Krejci, R., Petäjä, T., Percival, C., Davidovits, P., Worsnop, D. R., Ekman, A. M. L., Nenes, A., Martin, S., Jimenez, J. L., Collins, D. R., Topping, D. o., Bertram, A. K., Zuend, A., Virtanen, A., and Riipinen, I.: Microphysical explanation of the RH-dependent water affinity of biogenic organic aerosol and its importance for climate, Geophys. Res. Lett., 44, 5167–5177, https://doi.org/10.1002/2017GL073056, 2017.

Reddington, C. L., Morgan, W. T., Darbyshire, E., Brito, J., Coe, H., Artaxo, P., Scott, C. E., Marsham, J., and Spracklen, D. V.: Biomass burning aerosol over the Amazon: analysis of aircraft, surface and satellite observations using a global aerosol model, Atmos. Chem. Phys., 19, 9125–9152, https://doi.org/10.5194/acp-19-9125-2019, 2019.

Redemann, J., Wood, R., Zuidema, P., Doherty, S. J., Luna, B., LeBlanc, S. E., Diamond, M. S., Shinozuka, Y., Chang, I. Y., Ueyama, R., Pfister, L., Ryoo, J.-M., Dobracki, A. N., da Silva, A. M., Longo, K. M., Kacenelenbogen, M. S., Flynn, C. J., Pistone, K., Knox, N. M., Piketh, S. J., Haywood, J. M., Formenti, P., Mallet, M., Stier, P., Ackerman, A. S., Bauer, S. E., Fridlind, A. M., Carmichael, G. R., Saide, P. E., Ferrada, G. A., Howell, S. G., Freitag, S., Cairns, B., Holben, B. N., Knobelspiesse, K. D., Tanelli, S., L'Ecuyer, T. S., Dzambo, A. M., Sy, O. O., McFarquhar, G. M., Poellot, M. R., Gupta, S., O'Brien, J. R., Nenes, A., Kacarab, M., Wong, J. P. S., Small-Griswold, J. D., Thornhill, K. L., Noone, D., Podolske, J. R., Schmidt, K. S., Pilewskie, P., Chen, H., Cochrane, S. P., Sedlacek, A. J., Lang, T. J., Stith, E., Segal-Rozenhaimer, M., Ferrare, R. A., Burton, S. P., Hostetler, C. A., Diner, D. J., Seidel, F. C., Platnick, S. E., Myers, J. S., Meyer, K. G., Spangenberg, D. A., Maring, H., and Gao, L.: An overview of the ORACLES (ObseRvations of Aerosols above CLouds and their intEractionS) project: aerosol–cloud–radiation interactions in the southeast Atlantic basin, Atmos. Chem. Phys., 21, 1507–1563, https://doi.org/10.5194/acp-21-1507-2021, 2021.

Rickards, A. M. J., Miles, R. E. H., Davies, J. F., Marshall, F. H., and Reid, J. P.: Measurements of the Sensitivity of Aerosol Hygroscopicity and the κ Parameter to the O / C Ratio, J. Phys. Chem. A, 117, 14120–14131, https://doi.org/10.1021/jp407991n, 2013.

Ryoo, J.-M., Pfister, L., Ueyama, R., Zuidema, P., Wood, R., Chang, I., and Redemann, J.: A meteorological overview of the ORACLES (ObseRvations of Aerosols above CLouds and their intEractionS) campaign over the southeastern Atlantic during 2016–2018: Part 1 – Climatology, Atmos. Chem. Phys., 21, 16689–16707, https://doi.org/10.5194/acp-21-16689-2021, 2021.

Sedlacek, A. J., Lewis, E. R., Onasch, T. B., Zuidema, P., Redemann, J., Jaffe, D., and Kleinman, L. I.: Using the Black Carbon Particle Mixing State to Characterize the Lifecycle of Biomass Burning Aerosols, Environ. Sci. Technol., 56, 14315–14325, https://doi.org/10.1021/acs.est.2c03851, 2022.

Sheridan, P. J., Jefferson, A., and Ogren, J. A.: Spatial variability of submicrometer aerosol radiative properties over the Indian Ocean during INDOEX, J. Geophys. Res.-Atmos., 107, 8011, https://doi.org/10.1029/2000JD000166, 2002.

Shingler, T., Crosbie, E., Ortega, A., Shiraiwa, M., Zuend, A., Beyersdorf, A., Ziemba, L., Anderson, B., Thornhill, L., Perring, A. E., Schwarz, J. P., Campazano-Jost, P., Day, D. A., Jimenez, J. L., Hair, J. W., Mikoviny, T., Wisthaler, A., and Sorooshian, A.: Airborne characterization of subsaturated aerosol hygroscopicity and dry refractive index from the surface to 6.5 km during the SEAC4RS campaign, J. Geophys. Res.-Atmos., 121, 4188–4210, https://doi.org/10.1002/2015JD024498, 2016.

Suda, S. R., Petters, M. D., Matsunaga, A., Sullivan, R. C., Ziemann, P. J., and Kreidenweis, S. M.: Hygroscopicity frequency distributions of secondary organic aerosols, J. Geophys. Res.-Atmos., 117, D04207, https://doi.org/10.1029/2011JD016823, 2012.

Sumlin, B. J., Heinson, Y. W., Shetty, N., Pandey, A., Pattison, R. S., Baker, S., Hao, W. M., and Chakrabarty, R. K.: UV–Vis–IR spectral complex refractive indices and optical properties of brown carbon aerosol from biomass burning, J. Quant. Spectrosc. Ra., 206, 392–398, https://doi.org/10.1016/j.jqsrt.2017.12.009, 2018.

Thompson, G. and Eidhammer, T.: A Study of Aerosol Impacts on Clouds and Precipitation Development in a Large Winter Cyclone, J. Atmos. Sci., 71, 3636–3658, https://doi.org/10.1175/JAS-D-13-0305.1, 2014.

Titos, G., Cazorla, A., Zieger, P., Andrews, E., Lyamani, H., Granados-Muñoz, M. J., Olmo, F. J., and Alados-Arboledas, L.: Effect of hygroscopic growth on the aerosol

light-scattering coefficient: A review of measurements, techniques and error sources, Atmos. Environ., 141, 494–507, https://doi.org/10.1016/j.atmosenv.2016.07.021, 2016.

Titos, G., Burgos, M. A., Zieger, P., Alados-Arboledas, L., Baltensperger, U., Jefferson, A., Sherman, J., Weingartner, E., Henzing, B., Luoma, K., O'Dowd, C., Wiedensohler, A., and Andrews, E.: A global study of hygroscopicity-driven light-scattering enhancement in the context of other in situ aerosol optical properties, Atmos. Chem. Phys., 21, 13031–13050, https://doi.org/10.5194/acp-21-13031-2021, 2021.

van der Werf, G. R., Randerson, J. T., Giglio, L., Collatz, G. J., Mu, M., Kasibhatla, P. S., Morton, D. C., DeFries, R. S., Jin, Y., and van Leeuwen, T. T.: Global fire emissions and the contribution of deforestation, savanna, forest, agricultural, and peat fires (1997–2009), Atmos. Chem. Phys., 10, 11707–11735, https://doi.org/10.5194/acp-10-11707-2010, 2010.

Wang, J., Shilling, J. E., Liu, J., Zelenyuk, A., Bell, D. M., Petters, M. D., Thalman, R., Mei, F., Zaveri, R. A., and Zheng, G.: Cloud droplet activation of secondary organic aerosol is mainly controlled by molecular weight, not water solubility, Atmos. Chem. Phys., 19, 941–954, https://doi.org/10.5194/acp-19-941-2019, 2019.

Wang, W., Rood, M. J., Carrico, C. M., Covert, D. S., Quinn, P. K., and Bates, T. S.: Aerosol optical properties along the northeast coast of North America during the New England Air Quality Study–Intercontinental Transport and Chemical Transformation 2004 campaign and the influence of aerosol composition, J. Geophys. Res.-Atmos., 112, D10S23, https://doi.org/10.1029/2006JD007579, 2007.

Wu, H., Taylor, J. W., Szpek, K., Langridge, J. M., Williams, P. I., Flynn, M., Allan, J. D., Abel, S. J., Pitt, J., Cotterell, M. I., Fox, C., Davies, N. W., Haywood, J., and Coe, H.: Vertical variability of the properties of highly aged biomass burning aerosol transported over the southeast Atlantic during CLARIFY-2017, Atmos. Chem. Phys., 20, 12697–12719, https://doi.org/10.5194/acp-20-12697-2020, 2020.

Zhang, L., Sun, J. Y., Shen, X. J., Zhang, Y. M., Che, H., Ma, Q. L., Zhang, Y. W., Zhang, X. Y., and Ogren, J. A.: Observations of relative humidity effects on aerosol light scattering in the Yangtze River Delta of China, Atmos. Chem. Phys., 15, 8439–8454, https://doi.org/10.5194/acp-15-8439-2015, 2015.

Zhang, L., Segal-Rozenhaimer, M., Che, H., Dang, C., Sedlacek III, A. J., Lewis, E. R., Dobracki, A., Wong, J. P. S., Formenti, P., Howell, S. G., and Nenes, A.: Light absorption by brown carbon over the South-East Atlantic Ocean, Atmos. Chem. Phys., 22, 9199–9213, https://doi.org/10.5194/acp-22-9199-2022, 2022.

Zhang, Q., Jimenez, J. L., Canagaratna, M. R., Allan, J. D., Coe, H., Ulbrich, I., Alfarra, M. R., Takami, A., Middlebrook, A. M., Sun, Y. L., Dzepina, K., Dunlea, E., Docherty, K., DeCarlo, P. F., Salcedo, D., Onasch, T., Jayne, J. T., Miyoshi, T., Shimono, A., Hatakeyama, S., Takegawa, N., Kondo, Y., Schneider, J., Drewnick, F., Borrmann, S., Weimer, S., Demerjian, K., Williams, P., Bower, K., Bahreini, R., Cottrell, L., Griffin, R. J., Rautiainen, J., Sun, J. Y., Zhang, Y. M., and Worsnop, D. R.: Ubiquity and dominance of oxygenated species in organic aerosols in anthropogenically-influenced Northern Hemisphere midlatitudes, Geophys. Res. Lett., 34, L13801, https://doi.org/10.1029/2007GL029979, 2007.

Zieger, P., Fierz-Schmidhauser, R., Gysel, M., Ström, J., Henne, S., Yttri, K. E., Baltensperger, U., and Weingartner, E.: Effects of relative humidity on aerosol light scattering in the Arctic, Atmos. Chem. Phys., 10, 3875–3890, https://doi.org/10.5194/acp-10-3875-2010, 2010.

Zieger, P., Fierz-Schmidhauser, R., Weingartner, E., and Baltensperger, U.: Effects of relative humidity on aerosol light scattering: results from different European sites, Atmos. Chem. Phys., 13, 10609–10631, https://doi.org/10.5194/acp-13-10609-2013, 2013.

Zieger, P., Fierz-Schmidhauser, R., Poulain, L., Müller, T., Birmili, W., Spindler, G., Wiedensohler, A., Baltensperger, U., and Weingartner, E.: Influence of water uptake on the aerosol particle light scattering coefficients of the Central European aerosol, Tellus B, 66, 22716, https://doi.org/10.3402/tellusb.v66.22716, 2014.

Zieger, P., Aalto, P. P., Aaltonen, V., Äijälä, M., Backman, J., Hong, J., Komppula, M., Krejci, R., Laborde, M., Lampilahti, J., de Leeuw, G., Pfüller, A., Rosati, B., Tesche, M., Tunved, P., Väänänen, R., and Petäjä, T.: Low hygroscopic scattering enhancement of boreal aerosol and the implications for a columnar optical closure study, Atmos. Chem. Phys., 15, 7247–7267, https://doi.org/10.5194/acp-15-7247-2015, 2015.